Breaking Demodulation Limitations: AWG and Deep Learning in Dynamic Spectral Reconstruction for Differential FBG Accelerometers

Qian Yang, Lei Liu, Ning Niu, ChenYi Quan, SuFen Ren, ShengChao Chen, JiaLin Zhang, YuMeng Yan, LongTeng Xiang, YiPing Wang, ChangRui Liao, Jun He, and GuanJun Wang

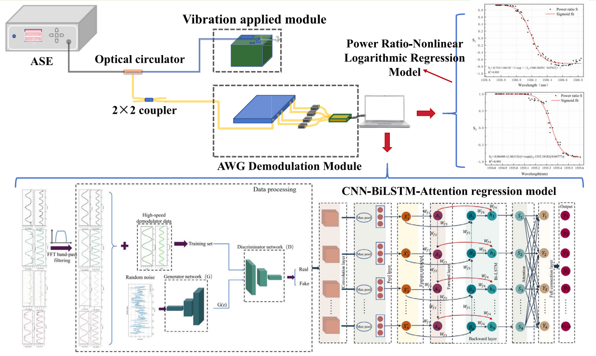

***Abstract*—The conventional fiber Bragg grating (FBG) accelerometer demodulation often suffers from high-environmental sensitivity, complexity, and cost. To address these issues, this article presents two arrayed waveguide grating (AWG)-based dynamic spectral reconstruction models. First, a novel differential FBG accelerometer with an equal-intensity triangular cantilever beam and a symmetric string-like design enhances sensitivity and mitigates temperature interference. A power ratio–nonlinear logarithmic regression (PR–NLR) model derived from static calibration then enables spectral reconstruction and wavelength demodulation across varying accelerations, achieving 4–82-pm accuracy, slightly below that of high-speed demodulators (HSDs). Next, by integrating convolutional neural network (CNN), bidirectional long short-term memory (BiLSTM), attention mechanisms, and a generative adversarial network (GAN) for data augmentation, prediction errors drop to 1–26 pm at 20 Hz and 0.2–21 pm at 40 Hz—a reduction of at least 60% over PR–NLR. This outcome underscores the advantages of deep learning (DL) in managing complex spectral shifts. By overcoming frequency-only demodulation limits, the proposed AWG approach achieves precise wavelength demodulation through dynamic spectral reconstruction. Its compact design, low manufacturing cost, and robust performance facilitate scalable deployment in structural health monitoring, particularly for bridge vibration analysis and industrial machinery diagnostics.**

***Index Terms*— Arrayed waveguide gratings (AWGs), attention, bidirectional long short-term memory (BiLSTM), convolutional neural network (CNN), dynamic spectral reconstruction, fiber Bragg grating (FBG), power ratio–nonlinear logarithmic regression (PR–NLR), wavelength demodulation.**

I. INTRODUCTION

FIBER Bragg gratings (FBGs) have emerged as prominent sensing elements in vibration measurement, due to their excellent electromagnetic compatibility, compact size, corrosion resistance, and ability to multiplex multiple sensing points over long distances [1], [2], [3], [4], [5]. When external strain or temperature fluctuations cause a Bragg wavelength shift in the fiber core, FBGs can accurately capture dynamic signals, making them invaluable for infrastructure monitoring, geological surveying, and motion detection [6], [7], [8].

Despite their promise, demodulation remains a bottleneck for widespread adoption. Phase demodulation via interferometers [9], such as Michelson (MI) [10] and Mach–Zehnder (MZI) [11], [12], achieves high sensitivity and a wide dynamic range but suffers from limited integration, high-temperature sensitivity, and stringent hardware demands [13], [14], [15].

The wavelength demodulation can directly obtain the Bragg wavelength shift using high-speed demodulators (HSD); yet, these are costly and bulky, restricting large-scale deployment [16], [17]. Various demodulation methods—charge-coupled device (CCD) spectral imaging [18], [19], tunable

Received 15 January 2025; revised 4 March 2025 and 31 March 2025; accepted 1 April 2025. Date of publication 10 April 2025; date of current version 2 June 2025. This work was supported in part by the Key Research and Development Plan of Hainan Province under Grant ZDYF2023GXJS013; in part by the National Natural Science Foundation of China under Grant 62175054; in part by the Major Science and Technology Program of Haikou City under Grant 2021-002; and in part by the Innovative Research Topics for Postgraduate Students in Hainan Province, China, under Grant SA2400003326. The associate editor coordinating the review of this article and approving it for publication was Dr. Anuj K. Sharma. *(Corresponding author: GuanJun Wang.)*

Please see the Acknowledgment section of this article for the author affiliations.

Digital Object Identifier 10.1109/JSEN.2025.3557684

Fabry–Pérot (F–P) filtering [20], tunable laser scanning [21], [22], and matched filtering [23]—have been explored to address these constraints. CCD spectral imaging offers broad wavelength coverage and high accuracy but suffers from complex optics and high cost. Tunable F–P filtering provides high resolution and wide tuning yet remains sensitive to vibrations and temperature drifts. Tunable laser scanning achieves precise wavelength control but faces slow scanning speeds and possible mode hopping. Matched filtering is hardware-simple for medium-to-low-speed demodulation but cannot accommodate large wavelength drifts beyond its linear range [24], [25]. A variable-step, high-speed demodulation scheme improves single-peak detection by reducing tuning steps [26], though it is still complex and untested for multigrating setups. An on-chip approach using cascaded microring resonators (MRRs) enables multichannel, low-cost, high-speed demodulation, but MRR fabrication precision remains a bottleneck [27]. Consequently, developing a compact, robust dynamic demodulation system that balances performance and cost is crucial for real-world engineering applications.

Within the matched filtering category, arrayed waveguide gratings (AWGs) provide multichannel spectral distribution and integrated photonic fabrication, expanding both the wavelength measurement range and the operating bandwidth [28]. They remain compact and energy efficient at higher frequencies, offering a scalable option for dynamic FBG demodulation [29], [30]. Prior studies combining AWGs with semiconductor ring lasers achieved microstrain measurements at frequencies up to 120 kHz but primarily focused on frequency extraction rather than real-time wavelength demodulation for parameters such as acceleration [31], [32].

Meanwhile, deep learning (DL) has demonstrated excellence in high-dimensional feature extraction and temporal dependency analysis under resource constrained or complex conditions [33]. For instance, a random forest-based approach achieved a root mean square error (RMSE) of 0.73 pm [34], while Transformer-based cascaded networks reduced errors to 1 pm [35]. However, these methods exhibit three fundamental shortcomings in dynamic environments [36], [37].

1) *Temporal Dependency Neglect:* Unidirectional models [e.g., long short-term memory (LSTM)] fail to capture bidirectional vibration phase interactions (e.g., compression–tension cycles in cantilever beams).
2) *Noise Susceptibility:* Raw AWG channel signals often embed high-frequency noise from photodetectors (PDs) and light source fluctuations.
3) *Data Scarcity:* Small-sample conditions in real-world deployments limit model generalization across varying frequencies and accelerations.

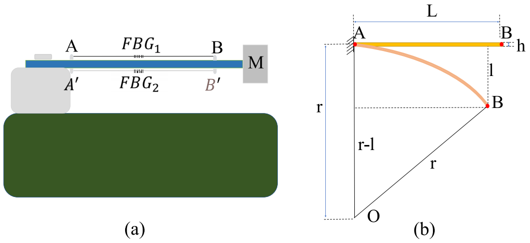

Fig. 1. (a) Vibration test platform. (b) Schematic of equal-strength triangular cantilever beam bending.

To address these gaps, this work proposes a novel hybrid architecture combining a convolutional neural network (CNN), bidirectional LSTM (BiLSTM), and attention mechanisms, augmented with generative adversarial network (GAN)-based data augmentation. The CNN handles feature extraction, while the BiLSTM captures bidirectional temporal patterns, an approach shown to improve traffic [38] and cardiovascular health monitoring [39]. To overcome the BiLSTM's limited global context capture, we incorporate an attention mechanism, drawing on Ma et al.'s [40] findings, where a CNN–BiLSTM–Attention framework significantly improved the performance prediction of electrohydrostatic actuators. In addition, to address the challenge of large-scale data acquisition (DAQ), we employ a GAN with gated recurrent units (GRUs) for data augmentation, thereby increasing dataset diversity and enhancing model generalization. This approach uniquely integrates the following.

1) CNN for local spectral feature extraction and noise suppression.
2) BiLSTM to capture bidirectional temporal dependencies in vibration signals.
3) Attention mechanisms to dynamically focus on critical time steps, and GAN-generated synthetic data to overcome small-sample limitations in dynamic scenarios.

Experimental validation demonstrates an 89.93% reduction in mean absolute error (MAE) compared with static calibration methods [power ratio–nonlinear logarithmic regression (PR–NLR)] under dynamic conditions of 20–40 Hz and 0.2–1.2 g, with prediction errors as low as 0.2 pm at 40 Hz. This work advances the AWG-based fully-dynamic demodulation system by transitioning from mere frequency extraction to wavelength demodulation for parameters such as acceleration. By integrating spatiotemporal learning through attention mechanisms with GAN-based augmentation techniques, we have achieved dynamic wavelength demodulation of the AWG–FBG system. This method eliminates the reliance on HSDs, reduces costs, and provides a novel approach to intelligent fiber optic sensing for industrial and structural health monitoring applications.

II. THEORETICAL ANALYSIS AND DEMODULATION SCHEME

A. Working Principle and Sensor Design

1) Dual-FBG Differential Vibration Measurement Principle: Axial strain and temperature variations induce shifts in the central wavelength of the FBG, with bending effects ignored in this analysis. The FBG acceleration sensor employs an elastic element to convert vibration displacement into axial strain, enabling wavelength modulation. The elastic element is essential for transmitting vibration displacement. To minimize the chirp effect of the FBG, we designed an isosceles triangular cantilever beam with uniform strength.

Two FBG fiber arrays with central wavelengths of 1555 and 1560 nm were symmetrically installed using prestress and UV adhesive, forming a string-like structure, as shown in Fig. 1(a). The sensor's equivalent model, as depicted in Fig. 1(b), has a fixed end A and a free end B, with the curvature at point B calculated using the following equation [41]:

$$\frac{1}{r} = \frac{12FL}{Eb_0h^3} \tag{1}$$

where r is the bending radius of the cantilever beam, E is Young's modulus, L is the beam length, b_0 is the width at the fixed end, and h is the thickness. Under a constant force F, r remains unchanged. The axial strain ε of the cantilever beam is given by

$$\varepsilon = \frac{\Delta h}{r} \tag{2}$$

where $\Delta h = (1/2)h$ represents the distance from the specified surface to the neutral layer. Substituting Δh yields

$$\varepsilon = \frac{12FL\Delta h}{Eb_0h^3} = \frac{6FL}{Eb_0h^2} = \frac{6L}{Eb_0h^2} \cdot ma \tag{3}$$

where a denotes the acceleration and m is the mass at the free end. When the fixed end A undergoes vibrational excitation, the free end B experiences inertial forces, resulting in an approximately uniform axial strain distribution along the beam. The FBG sensing equations for the top and bottom surfaces are

$$\begin{aligned} \Delta\lambda_1 &= [(1 - P_e)\,\varepsilon_1 + K_{T1}\Delta T]\,\lambda_{\mathrm{FBG}_1} \\ \Delta\lambda_2 &= [(1 - P_e)\,\varepsilon_2 + K_{T2}\Delta T]\,\lambda_{\mathrm{FBG}_2} \end{aligned} \tag{4}$$

where $\Delta\lambda_1$ and $\Delta\lambda_2$ denote the central wavelength shifts, λ_{FBG_1} and λ_{FBG_2} are the (prestressed) nominal Bragg wavelengths, P_e is the effective elastic-optic coefficient, ε_1 and ε_2 are the axial strains of FBG$_1$ and FBG$_2$, respectively, and K_{T1} and K_{T2} are the temperature sensitivity coefficients. Since the FBG arrays are made of identical materials (and have similar parameters), it follows that $K_{T1} = K_{T2}$ and $\varepsilon_1 = -\varepsilon_2 = \varepsilon$. Thus, the difference in their central wavelengths is

$$\begin{aligned} \Delta\lambda_d &= \Delta\lambda_1 - \Delta\lambda_2 \\ &= (1 - P_e)\left(\lambda_{\mathrm{FBG}_1} + \lambda_{\mathrm{FBG}_2}\right) \cdot \varepsilon \\ &= (1 - P_e)\left(\lambda_{\mathrm{FBG}_1} + \lambda_{\mathrm{FBG}_2}\right) \cdot \frac{6L}{Eb_0h^2} Ma. \end{aligned} \tag{5}$$

Because $\Delta\lambda_d$ depends only on acceleration-induced strain (and not on uniform temperature changes), temperature interference is effectively canceled while the measurement sensitivity is significantly enhanced.

2) Design of Acceleration Sensor: The elastic element of the FBG vibration sensor is illustrated in Fig. 2(b). The FBGs are symmetrically mounted on the top and bottom surfaces of the cantilever beam, forming a stable "string-like" configuration. A mass block M is attached to the free end to enhance sensitivity. Under external vibration, inertial forces drive vertical oscillations of the free end.

Finite element simulations guided the design of the cantilever beam with optimized dimensions: length, $L = 30$ mm; width, $b = 15$ mm; thickness, $h = 0.3$ mm; and an effective FBG length of 20 mm. As shown in Fig. 2(a), the elastomer is fabricated from 65-Mn spring steel, and the mass block is made of structural steel. Modal analysis indicates a first natural frequency of 28.44 Hz and a sensitivity exceeding 0.6 nm/g with a 6-g mass block.

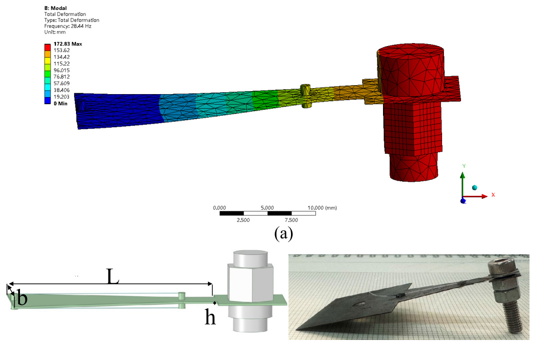

(a)

(b) (c)

Fig. 2. Accelerometer schematic. (a) First-order modal analysis showing resonance modes. (b) 3-D structural diagram of the dual-FBG sensor. (c) Photograph of the sensor.

B. Principle of Differential FBG Accelerometers Based on AWG

1) Demodulation System: Fig. 3(a) shows the AWG-based FBG wavelength demodulation system, which employs a relative intensity demodulation method. Because the system's output depends on the ratio of optical powers in adjacent channels, it remains unaffected by light source fluctuations and FBG bandwidth, thereby ensuring high demodulation accuracy. Light passes sequentially through FBG$_1$ and FBG$_2$ via an optical circulator. Wavelengths satisfying the Bragg condition are reflected and transmitted to the AWG.

The AWG translates wavelength shifts into transmitted light intensity variations through its wavelength division multiplexing capability. As shown in Fig. 3(b), the transmitted light intensity corresponds to the spectral overlap between the FBG reflection and AWG channel spectra. Here, λ_{FBG_1} and λ_{FBG_2} denote the central wavelengths of the FBGs, while CHN(i), CHN($i+1$), CHN($i+j$), and CHN($i+j+1$) represent the transmission spectra of AWG channels. The shaded regions W_i, W_{i+1}, W_{i+j}, and W_{i+j+1} indicate the transmitted light intensities in respective channels. Any shift in the FBG's central wavelength—caused by strain or temperature—changes the transmitted intensities. The relationship between the logarithmic optical power ratio of adjacent channels and the FBG central wavelength is given by [32]

$$\ln\left(\frac{W_{i+1}}{W_i}\right) = \frac{8(\ln 2)\Delta\lambda_c}{\Delta\lambda_{\mathrm{FBG}}^2 + \Delta\lambda_i^2}\lambda_{\mathrm{FBG}} - \frac{4\ln 2\left(\lambda_{i+1}^2 + \lambda_i^2\right)}{\Delta\lambda_{\mathrm{FBG}}^2 + \Delta\lambda_i^2} \tag{6}$$

where $\Delta\lambda_c$ is the central wavelength difference between channels, $\Delta\lambda_{\mathrm{FBG}}$ is the FBG's full-width at half-maximum (FWHM), and $\Delta\lambda_i$ and $\Delta\lambda_{i+1}$ are the FWHM of the i-th and $(i+1)$th channels, respectively. A PD array measures the transmitted intensities, which are processed by a DAQ card to demodulate FBG wavelength shifts.

2) Spectral Reconstruction Model Under Static Calibration: The static calibration principle converts vibration-induced strain into static fiber strain for system characterization.

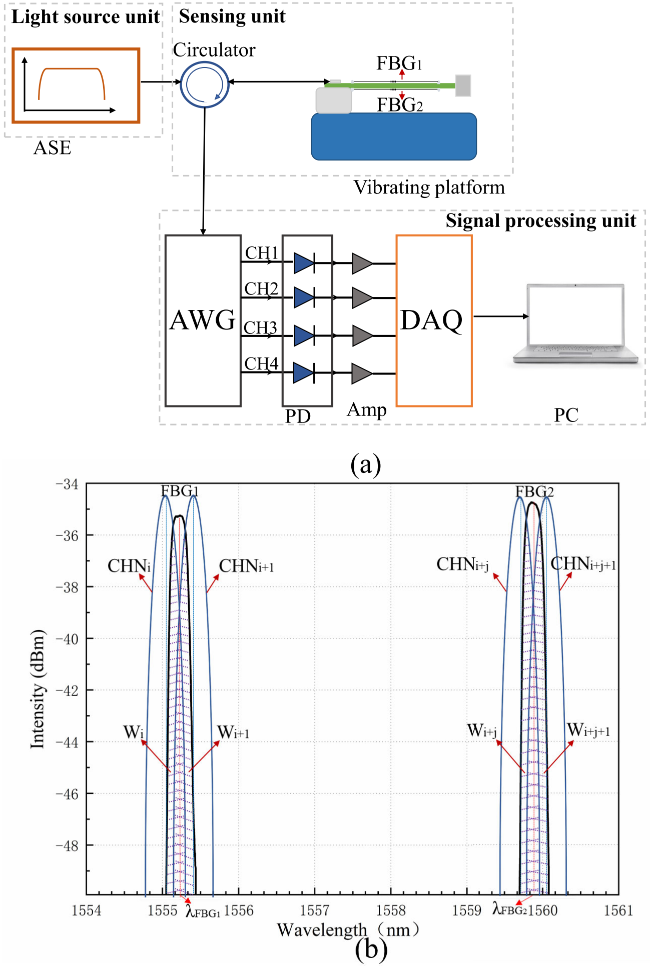

Fig. 3. AWG-based demodulation system and operating principle. (a) Schematic of the differential FBG accelerometer demodulation system. (b) Principle of the AWG demodulation method showing the overlap between AWG channel spectra and FBG reflection spectra.

As depicted in Fig. 4(a), the setup includes a 20-mW ASE light source, a 100-GHz AWG, an AK6140 optical spectrum analyzer (OSA), a 3-dB fiber coupler, and a 3-D displacement platform. Prestretched FBG_1 (central wavelength: 1560.15 nm) is positioned between AWG channels 21 (1560.592 nm) and 22 (1559.792 nm), while FBG_2 (1555.20 nm) is placed between channels 27 (1555.764 nm) and 28 (1554.948 nm).

The displacement platform applied reversible vertical deformation in 50-μm increments under simulated vibration. Static calibration established the relationship between AWG optical power and the FBG central wavelength. The OSA monitored strain-induced wavelength shifts, while the PD array recorded the AWG channel intensities. To suppress light source noise, the power ratio S was calculated as follows [17]:

$$S = \frac{W(i+1) - W(i)}{W(i+1) + W(i)}. \tag{7}$$

S is unaffected by insertion loss. The relationship between S and the FBG central wavelength can be described by a logarithmic function [38]

$$\lambda = \lambda_0 + d\lambda \cdot \ln\left(\frac{A_1 - S}{S - A_2}\right). \tag{8}$$

A nonlinear logarithmic fit of λ versus S yields a Sigmoid function (9). The calibration parameters λ_0, $d\lambda$, A_1, and A_2 are extracted, as shown in Fig. 4(b) and (c)

$$S = A_2 + \frac{A_1 - A_2}{1 + \exp\left(\frac{\lambda - \lambda_0}{d\lambda}\right)}. \tag{9}$$

Equation (9), serving as the inverse function of (8), enables the determination of the FBG central wavelength by calculating the power ratio S through adjacent AWG channel measurements. To mitigate temperature effects, strain is quantified using the wavelength difference between the dual FBGs. Fig. 4(d) and (e) demonstrates the FBG wavelength values demodulated via PR–NLR model, derived from optical power measurements of corresponding AWG channels. As shown in Fig. 4(f), the demodulated FBG wavelength differences (hollow markers) align closely with the actual values recorded by the OSA (solid markers). This strong agreement confirms the validity and feasibility of the AWG-based demodulation system for monitoring the dynamic responses of FBG sensors.

III. DEMODULATION EXPERIMENTS AND DISCUSSION

Fig. 5 illustrates the experimental setup for the differential FBG accelerometer demodulation system. The system comprises three key modules: an AWG demodulation module, a reference demodulation module (HSD-based), and a vibration excitation module. A vibration operating system (JX-3) generates controlled vibrations with frequencies up to 1000 Hz and adjustable acceleration levels. A broadband light source illuminates the FBG, and the reflected signal is routed through a 2 × 2 fiber coupler to the AWG, ensuring consistent optical power matching static calibration conditions. The PD captures the optical signal, which is digitized by a DAQ. An HSD provides reference measurements with a sampling rate of 1 kHz and a resolution of 1 pm. The demodulated results from the AWG system are validated against HSD measurements, confirming the accuracy and robustness of the spectral reconstruction model.

A. Spectral Reconstruction of Acceleration at the Same Frequency

Measuring the wavelength differences caused by varying accelerations at the same frequency is a key indicator for assessing the sensitivity of the demodulation system, reflecting its capability to respond to minor changes in acceleration. As shown in Fig. 6(a), (c), (e), and (f), the HSD-recorded wavelength shifts of FBG_1 (1560.15 nm) and FBG_2 (1555.20 nm) over a 150-ms time window, while the AWG exhibited corresponding optical power variations in channels 21 and 27. Conversely, as shown in Fig. 6(b), (d), (e), and (f), channels 22 and 28 displayed inverse power trends, aligning with the static calibration results [Fig. 4(d) and (e)]. These observations confirm the AWG's capability to dynamically track wavelength shifts through complementary channel responses.

To mitigate temperature-induced interference, acceleration is quantified using wavelength differences between dual FBGs.

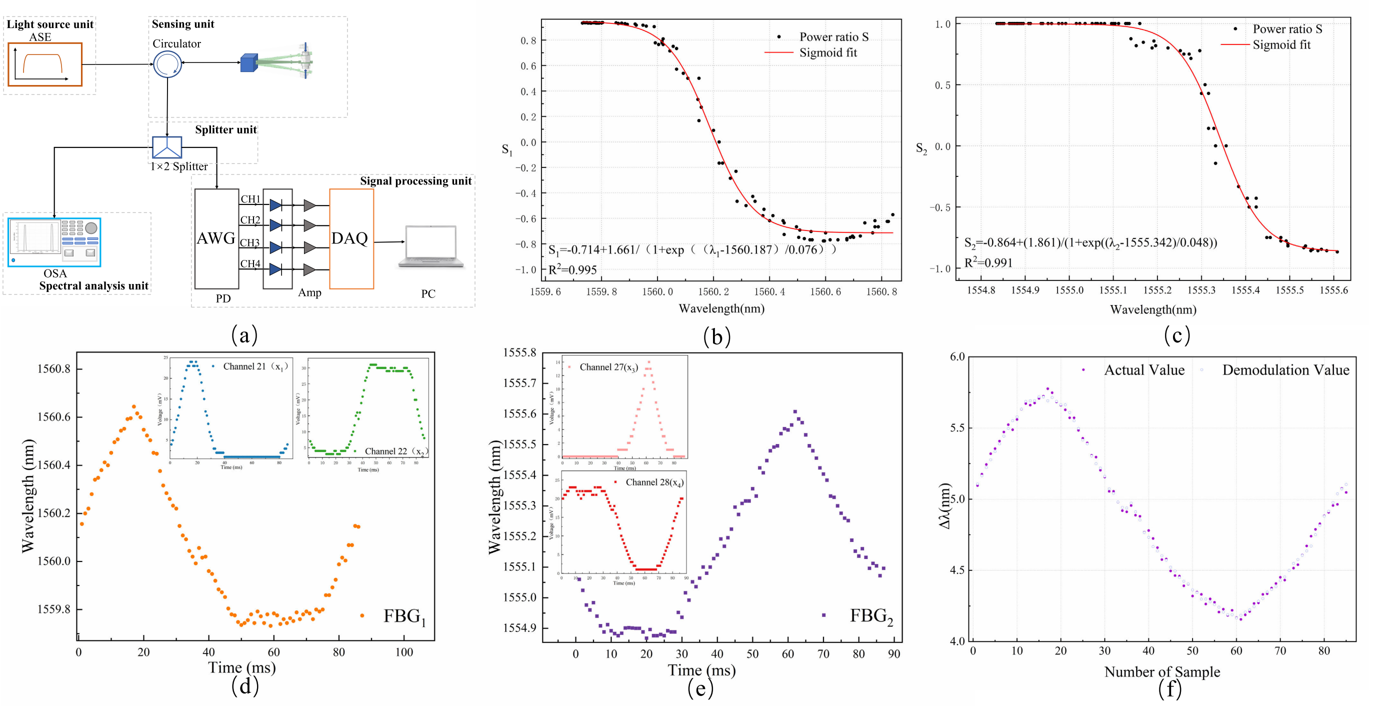

Fig. 4. Static calibration and spectral reconstruction validation of the AWG–FBG system. (a) Experimental setup for static calibration. (b) PR–NLR model fitting for FBG$_1$ ($\lambda_0 = 1560.187$ nm and $R^2 = 0.995$). (c) PR–NLR model fitting for FBG$_2$ ($\lambda_0 = 1555.342$ nm and $R^2 = 0.991$). (d) Spectral response of FBG$_1$ demodulated from AWG channels 21 and 22. (e) Spectral response of FBG$_2$ demodulated from AWG channels 27 and 28. (f) Comparison of wavelength differences measured by OSA and AWG, illustrating the excellent agreement for dynamic demodulation.

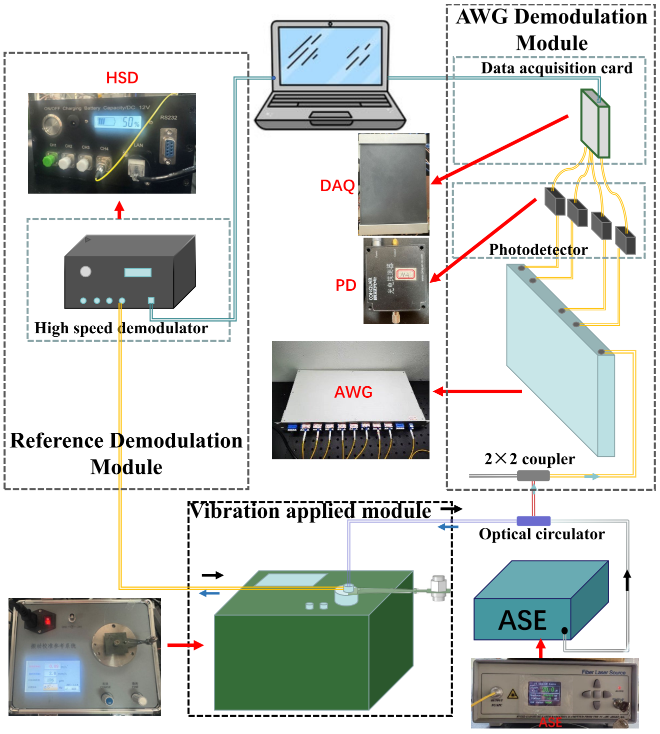

Fig. 5. Experimental setup for AWG-based differential FBG accelerometer demodulation.

Fig. 7(a) and (d) shows the comparison of the wavelength differences demodulated by the HSD and AWG (PR–NLR model) systems under accelerations of 0.2–1.2 g at 20 Hz. As shown in Fig. 7(b), (c), (e), and (f), detailed analyses of peak-to-valley amplitudes reveal high consistency between the two methods, with a maximum deviation of 0.0823 nm. The AWG demodulation exhibits rapid response to dynamic signals, as illustrated in Fig. 8, achieving a sensitivity of 730 pm/g. The close alignment of AWG-demodulated data points with the fit line demonstrates its consistency and stability relative to the HSD. A few points outside the confidence interval reflect model errors in AWG, primarily due to the static calibration model used for dynamic demodulation, which is more prominent at higher accelerations. These errors are minor, limited to a few points, and have minimal impact on actual measurements. Therefore, AWG is well-suited for applications requiring moderate accuracy and cost efficiency, such as industrial vibration and structural health monitoring. For consistency, all linearity and error evaluations in this article are based on wavelength difference valley.

B. Spectral Reconstruction of the Same Acceleration at Different Frequencies

To assess the system's capability to resolve rapidly varying signals, we evaluated its demodulation performance at a fixed acceleration of 0.4 g across multiple frequencies (10, 20, and 40 Hz). Fig. 9 illustrates a comparison of AWG spectral reconstruction and HSD measurement under different vibration frequencies (10, 20, 40 Hz) and a constant acceleration of 0.4 g. Fig. 9(a) demonstrates close alignment between HSD- and AWG-demodulated peak/valley values across frequencies, confirming system consistency. Fig. 9(b)–(g) provides the detailed comparisons, highlighting the differences in peaks and valleys between the two demodulation schemes. Fig. 10

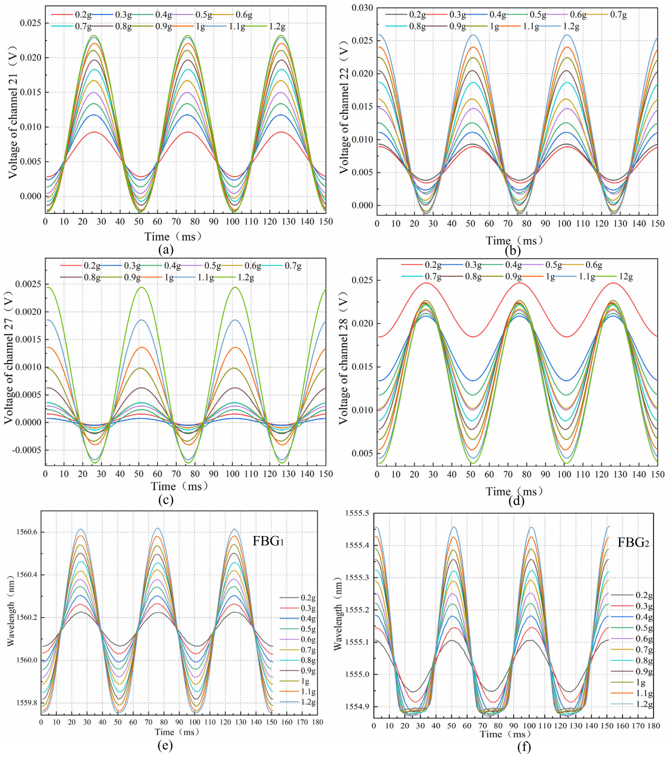

Fig. 6. Dynamic optical power response of AWG channels and HSD-recorded FBG wavelength shifts under 20-Hz vibration with varying accelerations (a) AWG channel 21 optical power versus acceleration: optical power trends align with wavelength shifts of FBG_1. (b) AWG channel 22 optical power versus acceleration: negatively correlated trends with FBG_1 wavelength shifts. (c) AWG channel 27 optical power versus acceleration: optical power trends align with wavelength shifts of FBG_2. (d) AWG channel 28 optical power versus acceleration: negatively correlated trends with FBG_2 wavelength shifts. (e) HSD-recorded FBG_1 wavelength dynamics: wavelength shifts under 0.2–1.2-g accelerations at 20 Hz. (f) HSD-recorded FBG_2 wavelength dynamics: Wavelength shifts under 0.2–1.2-g accelerations at 20 Hz.

presents the Fourier spectra of AWG-demodulated signals, demonstrating the AWG system's precise frequency capture and demodulation capability.

C. Different Acceleration Demodulations for Different Frequencies

The standard deviation serves as a metric for evaluating demodulation precision under varying conditions, where smaller values indicate higher consistency and reliability. Fig. 11(a) displays error bars and fit curves comparing AWG- and HSD-demodulated wavelength difference valleys across accelerations (0.2–1.2 g) and frequencies (10–40 Hz). The shaded regions represent 95% confidence intervals, indicating the range of error distribution. The line corresponds to the HSD reference fit. Most AWG error bars exhibit a small deviation from the HSD trendline (<0.8 g), demonstrating strong agreement between the two methods. Fig. 11(b) summarizes the error statistics, showing uniform distributions across frequencies, which confirms the stability of the AWG model. At higher accelerations (e.g., 1.1–1.2 g at 20 Hz and 0.9 g at 40 Hz), errors increase marginally (up to 0.0823 nm), likely due to the static calibration model's limitations in adaptability under such conditions. This suggests that the AWG system is more suitable for low-to-moderate acceleration ranges.

Fig. 12 shows the comparison of the trends in acceleration sensitivity for the HSD and AWG systems. Due to equipment limitations, the tests were restricted to specific frequencies available on the vibration table. The sensor exhibits higher sensitivity in the low-to-mid-frequency range, peaking at 750 pm/g at 20 Hz, which is close to its natural frequency of 28 Hz, consistent with the simulation results shown in Fig. 2(a). Sensitivity declines at frequencies above 80 Hz, which is attributed to mechanical resonance damping and structural rigidity constraints. Despite these limitations, both systems exhibit nearly identical sensitivity profiles, validating the reliability of the AWG model (PR–NLR) across the tested range.

IV. DL ALGORITHM FOR ACCELEROMETER SPECTRAL PREDICTION

A. Prediction Modeling

1) Data Augmentation: DL models often require large datasets, which makes data collection both time consuming and labor intensive. To improve generalization, we propose using a GAN-based data augmentation algorithm to expand training samples, increase data diversity, and preserve data integrity. This algorithm consists of a generator (G) and a discriminator (D), as shown in Fig. 13(a). The G network generates synthetic samples from random noise (z) to deceive D, while the D network is tasked with distinguishing between real and generated data. The detailed architecture, as depicted in Fig. 13(b), includes the embedding and recovery paths, the generator network (G), and the discriminator network (D). The network integrates GRUs to process sequential data and capture temporal dependencies. The embedding and recovery paths utilize linear and GRU layers to encode the original data into latent space representations and recover it. The G network generates latent space data from random noise, producing synthetic time series through GRU and linear layers. G and D are trained in a "min–max" framework, as described in the following equation [42]:

$$\min_G \max_D V(D,G) = E_{x\sim p_{\text{data}}(x)}\left[\log D(x)\right] + E_{z\sim p_z(z)}\left[\log\left(1 - D(G(z))\right)\right]. \quad (10)$$

Here, $D(X)$ denotes the discriminator, $G(z)$ represents the generator, p_{data} is the real data distribution, and p_z denotes the noise distribution. G and D iteratively optimize their performance through adversarial training until a Nash equilibrium is reached. This process allows $G(z)$ to generate realistic time-series data while simultaneously improving $D(X)$'s ability to distinguish between real and fake data.

2) CNN–BILSTM–Attention: Fig. 14 depicts the workflow and architecture of the spectral reconstruction model. The dataset is split into training and testing sets at an 8:2 ratio, with augmented data mixed, shuffled, and normalized with the training set. The model inputs include light intensities from four AWG channels and FBG wavelength difference spectra, forming time-series data with dimensions (BatchSize, 150, 5),

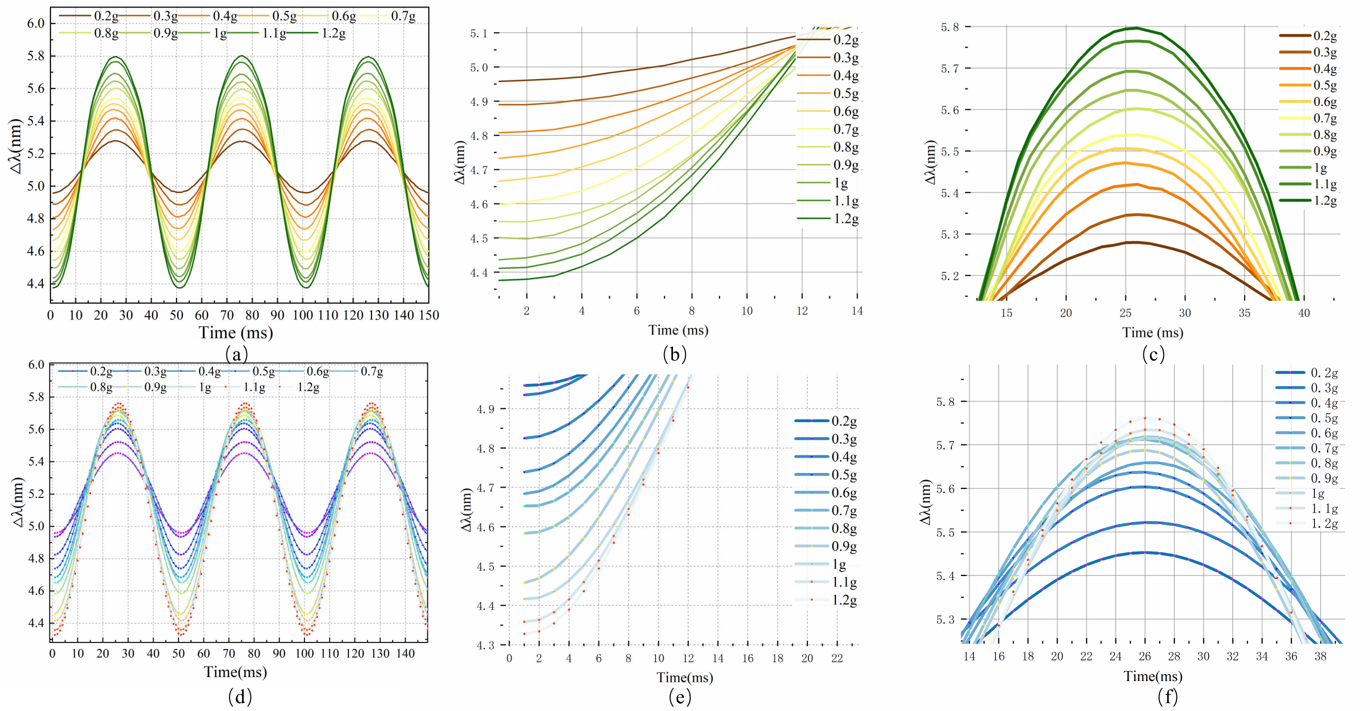

Fig. 7. Dynamic wavelength demodulation of differential FBG accelerometer via HSD- and AWG-based PR–NLR model. (a) HSD-measured FBG wavelength difference. (b) Magnified valley region of (a). (c) Magnified peak region of (a). (d) AWG-demodulated wavelength difference (PR–NLR model): reconstructed spectra aligned with HSD references, validating dynamic demodulation consistency. (e) Magnified valley region of (d). (f) Magnified peak region of (d).

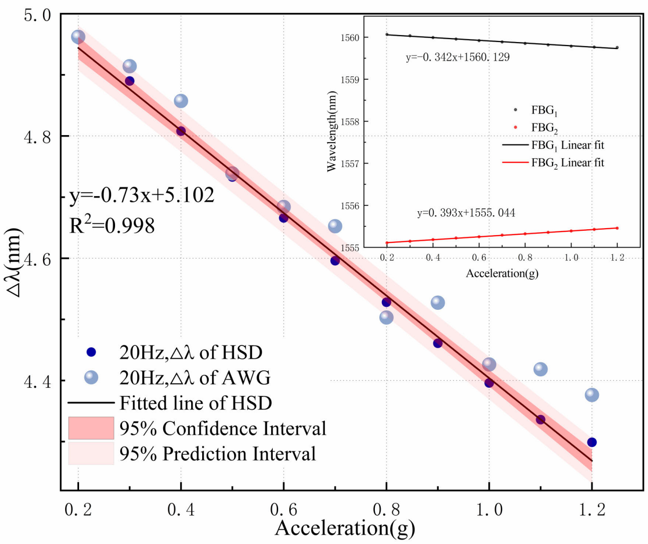

Fig. 8. Distribution of valley values for the HSD wavelength difference and the AWG-reconstructed spectral wavelength difference under 20-Hz vibration acceleration.

where 150 denotes the sequence length and 5 denotes the feature dimensions. An autoregressive model is used to predict FBG wavelength differences induced by varying accelerations under 20- or 40-Hz excitation conditions. Initially, the 1-D convolutional layer (Conv1D, kernel_size = 1, filters = 64, stride = 1, padding = valid, and activation = relu) performs dual functions: localized feature extraction from waveforms and high-frequency noise suppression originating from AWG channels, including PD thermal noise and light source fluctuations. The CNN layer effectively mitigates noise interference through its spatial filtering capability while preserving inherent signal characteristics. Subsequently, a BiLSTM (hidden units = 64, activation functions = “tanh” and “sigmoid”) addresses two critical challenges through its dual functionality.

1) *Temporal Pattern Capture:* Forward–backward sequence processing yields output dimensions of (BatchSize, 150, 128) while preventing overfitting via dropout regularization (rate = 0.3).
2) *Dynamic Environmental Adaptation:* Bidirectional physical dependencies (e.g., cantilever beam hysteresis effects) are modeled to enhance robustness.

This architecture demonstrates superior temporal modeling over unidirectional LSTM through coupled memory gates and reverse sequence analysis.

Next, the attention mechanism (attention_3d_block) applies learnable weights to each time step and feature, enhancing transient pattern recognition. Let the input sequence from the BiLSTM layer be $H \in R^{B\times T\times D}$, where B, T, and D represent the batch size, time steps, and feature dimensions, respectively. As depicted in Fig. 14, the attention module generates a learnable query vector $q \in R^{D}$, which interacts with H through a dense layer to compute compatibility scores

$$S = HW_i + b_i \tag{11}$$

where $W_i \in R^{D\times 1}$ and $b_i \in R^{T}$ are the trainable parameters. Attention weights $A \in R^{B\times T}$ are derived via softmax normalization

$$A = \mathrm{Softmax}(S). \tag{12}$$

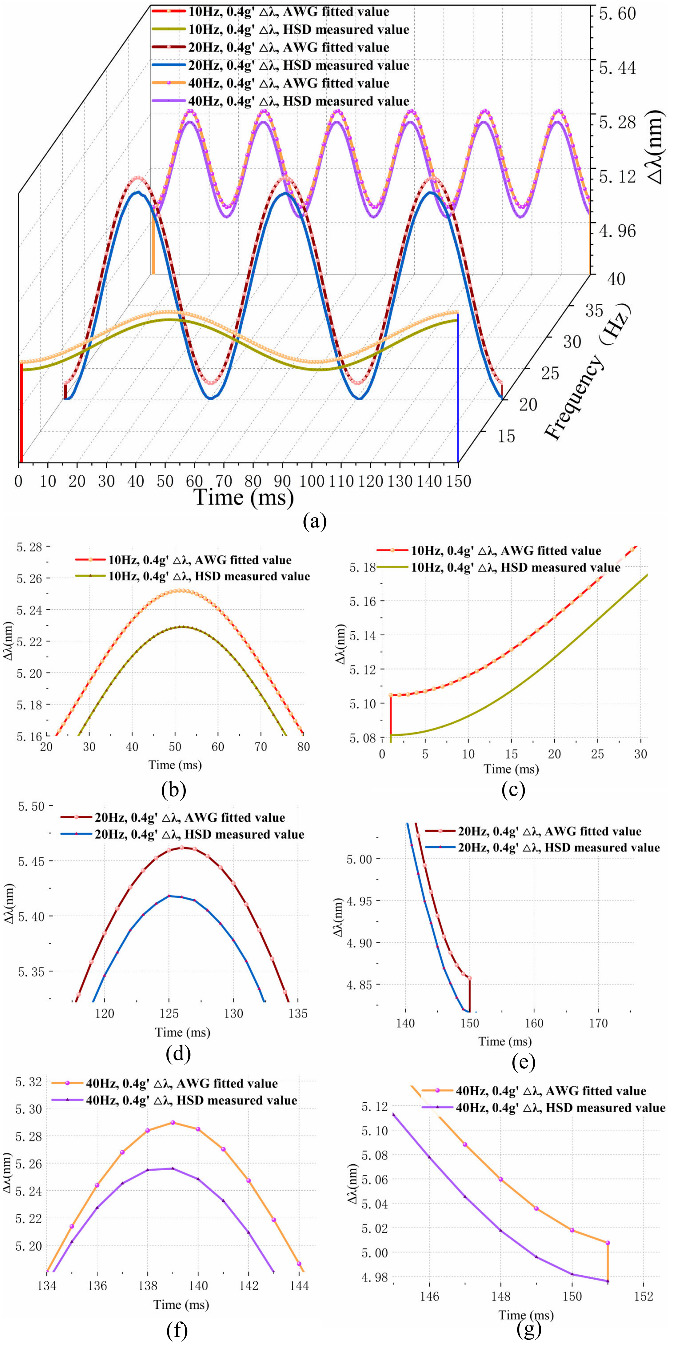

Fig. 9. Comparison of AWG spectral reconstruction and HSD demodulation under 0.4-g acceleration at varying frequencies. (a) Full-spectrum consistency: HSD versus AWG peak/valley alignment (10–40 Hz). (b) and (c) 10-Hz time-domain detailed plot: peak–valley dynamics. (d) and (e) 20-Hz time-domain detailed plot: peak–valley dynamics. (f) and (g) 40-Hz time-domain detailed plot: peak–valley dynamics.

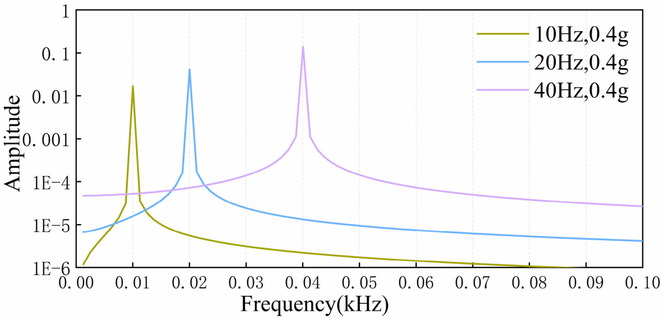

Fig. 10. Frequency characteristics of reconstructed spectra.

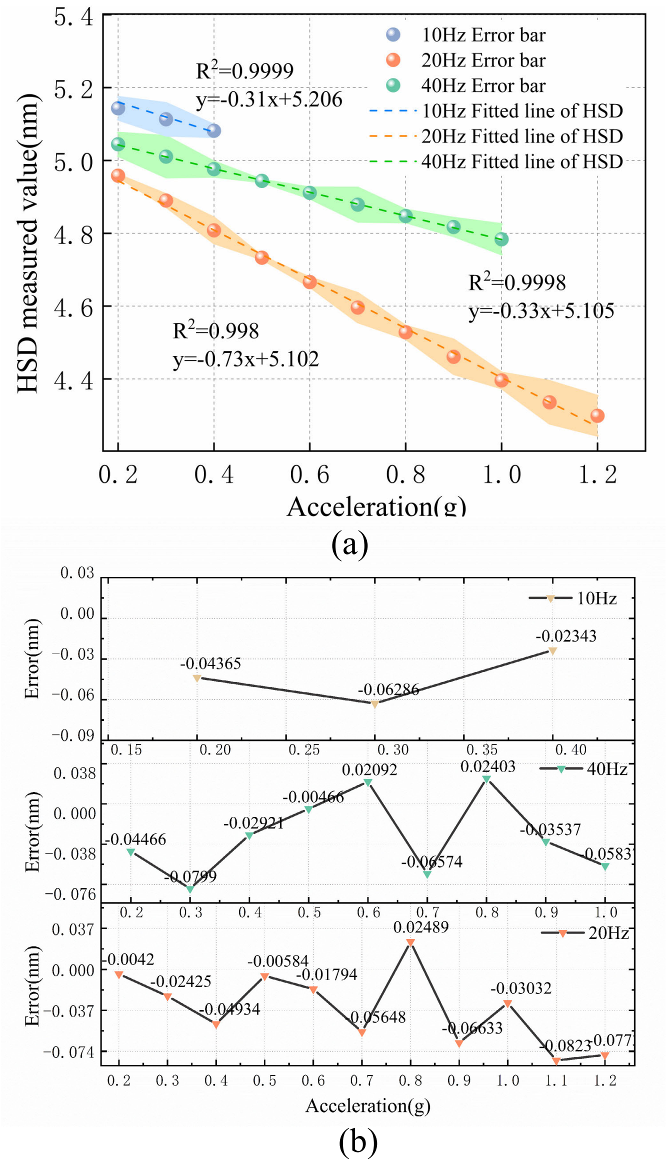

Fig. 11. Error analysis of AWG-demodulated wavelength differences under varying accelerations and frequencies. (a) Error bar distribution: confidence intervals (shaded) and HSD-fit curves for valley values (0.2–1.2 g, 10–40 Hz). (b) Error statistics of AWG- versus HSD-demodulated spectral valley differences under varying frequencies and accelerations.

The output $Z \in R^{B\times D}$ aggregates time-step features through weighted summation

$$Z = \sum_{t=1}^{T} A_{:,t} \odot H_{:,t,:} \tag{13}$$

where $\odot$ denotes the elementwise multiplication. As illustrated in Fig. 14, this process enables dual functionality.

1) Dynamic temporal weighting adaptively amplifies critical acceleration phases (e.g., peaks/valleys) while attenuating measurement artifacts through A, which assigns higher weights to discriminative time steps.
2) Multiscale feature prioritization enhances transient pattern recognition by modeling cross-dimensional

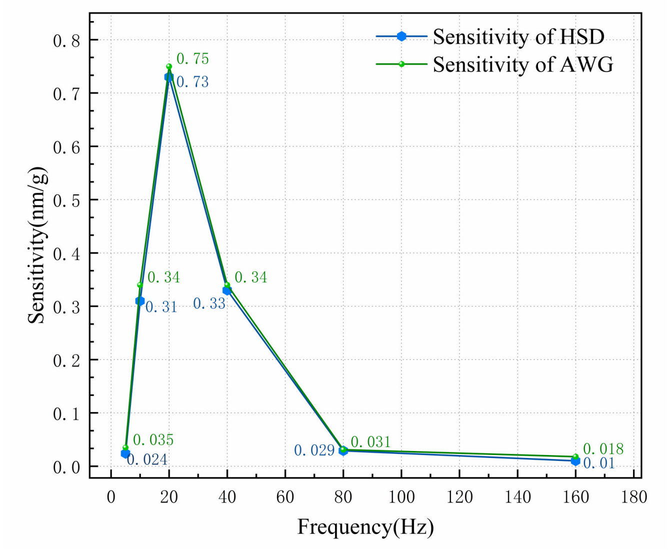

Fig. 12. Statistical comparison of HSD versus AWG sensitivity at different frequencies and accelerations.

correlations between BiLSTM outputs and attention-refined features.

Finally, flatten and dense layers transform data dimensions and output the predicted FBG wavelength differences.

B. Experiment and Discussion

1) DAQ: DAQ was carried out using the acceleration demodulation system shown in Fig. 5, which was employed to collect the transmitted light intensities from four AWG channels and the peak wavelengths of the FBGs. At both 20 and 40 Hz, HSD was used to obtain peak values from the FBG array and to perform differential processing, as depicted in Fig. 7(a). The spectral data from the AWG channels are presented in Fig. 6. Each periodic signal was recorded for 150 ms.

The acquisition frequencies and acceleration ranges were constrained by the vibration table's operational limits. To ensure consistent resolution and comprehensive data, acceleration datasets were collected at 20 and 40 Hz. Specifically, the acceleration range spanned from 0.02 to 1.2 g at 20 Hz and from 0.2 to 1.0 g at 40 Hz. Using a step size of 0.01 g, a total of 238 datasets were collected at 20 Hz and 180 datasets at 40 Hz.

2) Synthetic Data Generation: This article collected 418 spectral datasets across two distinct frequencies (20 and 40 Hz) and varying acceleration levels. To augment data diversity and improve model generalizability, a GAN, developed in Python using the TensorFlow framework, was implemented to generate synthetic spectral data. Fig. 15 shows the comparisons the original and synthetic data, showing that the synthetic data closely mirrors the original data in both waveform and amplitude distribution.

To quantitatively evaluate the GAN's performance, principal component analysis (PCA) and t-distributed stochastic neighbor embedding (t-SNE) were employed to compare feature distributions between original (red) and synthetic (blue) datasets. PCA preserved discriminative spectral features while filtering high-frequency noise, whereas t-SNE visualized the intrinsic clustering patterns. As shown in Fig. 16(a), the PCA projection reveals significant overlap in the principal component subspace between original and synthetic data, indicating that the GAN successfully captured the statistical distribution of the spectral data. The t-SNE visualization in Fig. 16(b) further supports this conclusion, as the synthetic data points integrate well with the original data points. Minor isolated clusters (e.g., pure red or blue points at the periphery) likely arise from stochastic variations during GAN training.

3) Model Training and Validation: The original dataset, consisting of 418 samples, was split into 80% for training (of which 10% was reserved for validation) and 20% for testing. The CNN–BiLSTM–Attention model was trained on a hybrid dataset consisting of 2508 samples, which included approximately 301 original samples drawn from the training set and 2207 synthetic samples generated by a GAN. The validation set was employed to evaluate model performance, fine-tune hyperparameters, and save the best-performing model using callback functions during testing.

The model architecture was implemented using TensorFlow's Keras API within a Python 3.9 and Anaconda environment and trained on a GeForce RTX 3050 Ti Max-Q GPU (8 GB). Key training parameters included 100 epochs, a batch size of 64, the Adam optimizer (default learning rate: 0.001), and mean squared error (mse) as the loss function. As shown in Fig. 17, the training and validation losses decreased rapidly during initial epochs and stabilized thereafter, demonstrating effective feature extraction without overfitting.

Figs. 18 and 19 show the comparison of the valley error distributions of the model trained on the original dataset (without synthetic data) and the hybrid dataset (augmented with GAN-generated data) under 20- and 40-Hz conditions, respectively. For 20 Hz, the test error range decreased from 4–78 pm (original dataset) to 1–26 pm (hybrid dataset). Similarly, at 40 Hz, the error range improved from 7–80 pm (original) to 0.2–21 pm (hybrid). The integration of synthetic data enabled the model to learn comprehensive temporal dynamics and noise resilience, significantly reducing maximum errors and stabilizing performance. These results validate the efficacy of data augmentation in enhancing spectral prediction accuracy.

Table I further quantifies the performance gains enabled by the DL framework. At 20 Hz, the maximum error decreases by approximately 65% (from 8.23×10^{-2} to 2.897×10^{-2} nm), and the mean error reduces by 77% (from 3.99×10^{-2} to 0.91152×10^{-2} nm). At 40 Hz, the maximum error drops by 73% (from 7.99×10^{-2} to 2.178×10^{-2} nm), with the mean error decreasing by 75%. This quantitative evidence underscores the DL model's ability to enhance sensor data perception by reducing errors and improving stability, leveraging synthetic data to mitigate noise and capture complex dynamics more effectively than non-DL methods.

Figs. 20 and 21 show the comparison of the model's predicted and actual values for the hybrid dataset. A mixed test set using 20- and 40-Hz acceleration data was employed

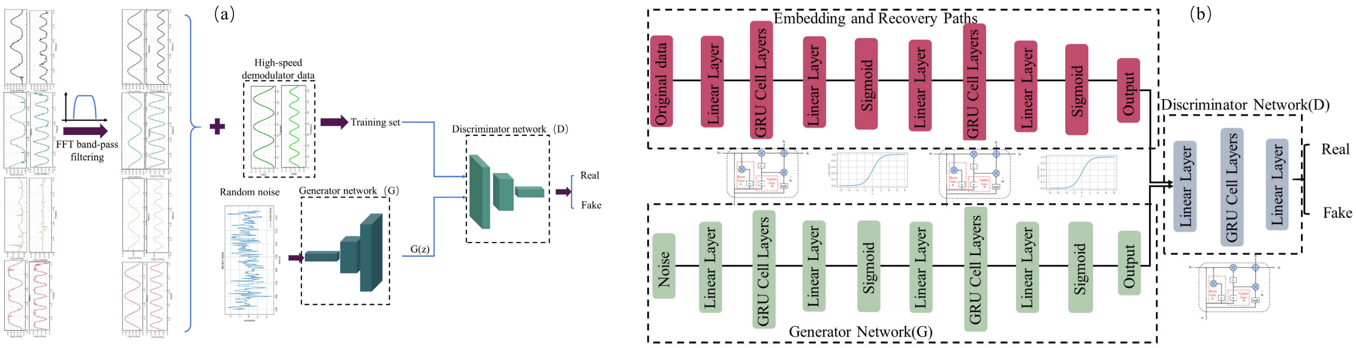

Fig. 13. Architecture and workflow of the GAN-based data augmentation framework. (a) Schematic of data augmentation using a GAN: The framework consists of a generator (*G*) and a discriminator (*D*). The *G* generates synthetic samples from random noise to deceive *D*, which is responsible for distinguishing between real and generated data. (b) Detailed architecture of the GAN: the network architecture includes embedding and recovery paths, as well as the *G* and *D* networks. GRUs are employed for sequence processing and capturing temporal dependencies. The *G* network synthesizes time series from noise through GRU and linear layers, while the *D* network distinguishes between real and generated data.

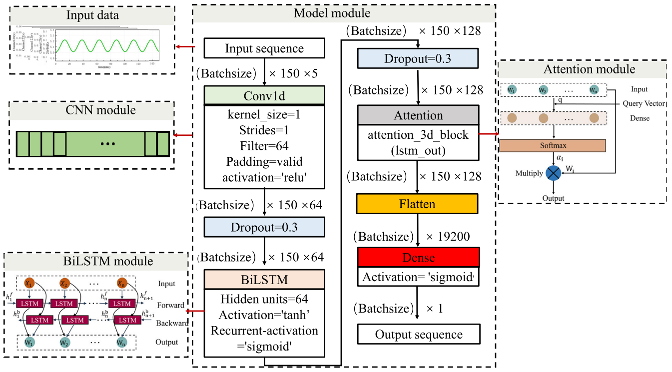

Fig. 14. Architecture of a DL model integrating CNN and BiLSTM with attention mechanism. The model processes time-series data through a CNN module for feature extraction, followed by a BiLSTM module to capture temporal dependencies. An attention mechanism is applied to enhance the model's focus on relevant features. The output is passed through a dense layer to produce the final prediction.

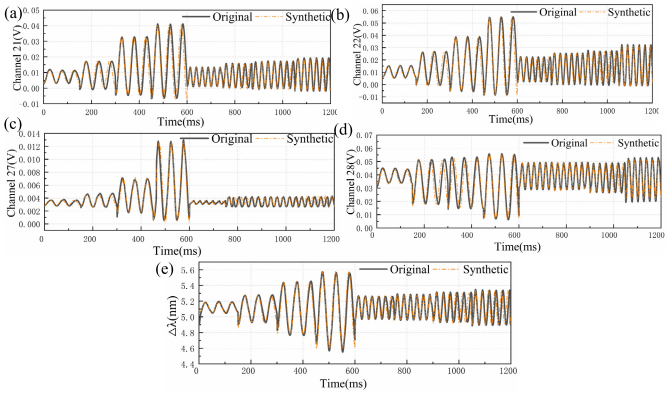

Fig. 15. Comparison of partially original and synthetic spectral data. (a)–(d) Partially synthetic and original spectral waveforms for AWG channels 21, 22, 27, and 28 at 20 and 40 Hz. (e) Partially synthetic and original wavelength difference profiles for FBG sensors at 20 and 40 Hz.

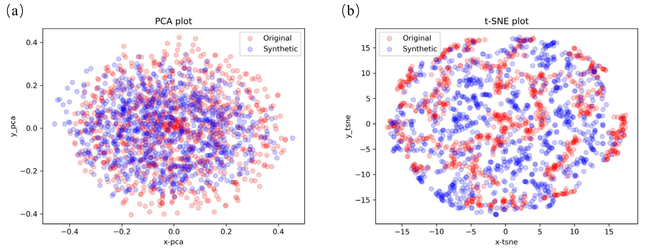

Fig. 16. Dimensionality reduction analysis of original (red) and synthetic (blue) spectral data. (a) PCA projection showing overlapping distributions in principal component space. (b) t-SNE visualization illustrating integration of synthetic and original clusters.

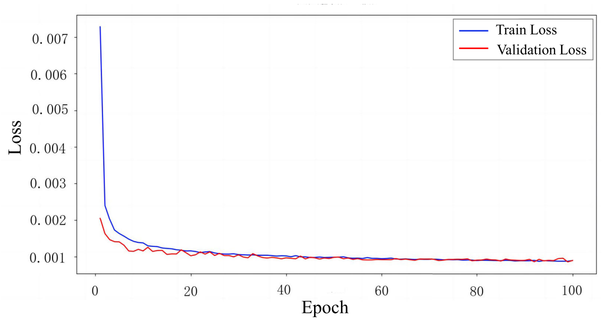

Fig. 17. CNN–BiLSTM–Attention model training and validation curves based on GAN [18].

TABLE I
COMPARISON OF PR–NLR AND CNN–BI–LSTM–ATTENTION MODELS IN ERROR AT 20 AND 40 Hz

Model	Frequency (Hz)	Maximum Error $(\times 10^{-2} nm)$	Minimum Error $(\times 10^{-3} nm)$	Mean Error $(\times 10^{-2} nm)$
PR-NLR	20	8.23	4.2	3.99
	40	7.99	4.7	4.03
CNN-BiLSTM-Attention	20	2.897	0.97	0.91152
	40	2.178	0.2	0.9877143

to validate the model's generalization capabilities on unseen data. The close alignment between the predicted and actual spectra highlights the model's high accuracy. The prediction fit at 20 Hz is superior to that at 40 Hz, likely due to the higher sensitivity at 20 Hz, enabling the model to capture the spectral patterns more effectively at this frequency. In addition, the poorer fit at smaller accelerations may be due to weaker signal strength and a lower signal-to-noise ratio. The improved fit with higher accelerations further supports this analysis.

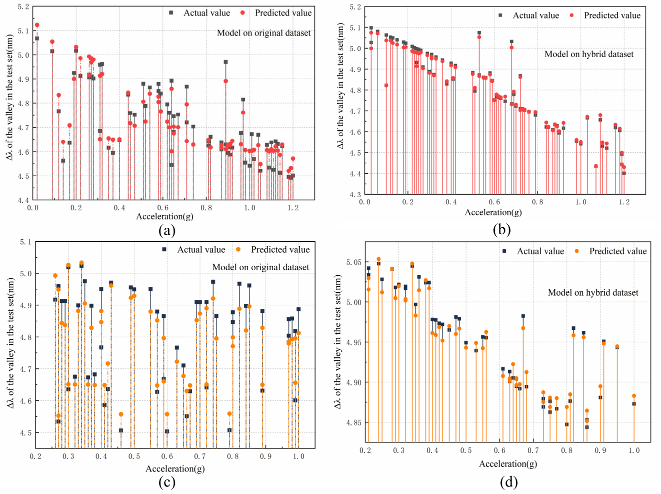

Fig. 18. Predicted and actual valley comparison at 20 and 40 Hz for original versus hybrid datasets. (a) and (b) Comparison of spectral predictions for original and hybrid datasets at 20 Hz. (c) and (d) Comparison of spectral predictions for original and hybrid datasets at 40 Hz.

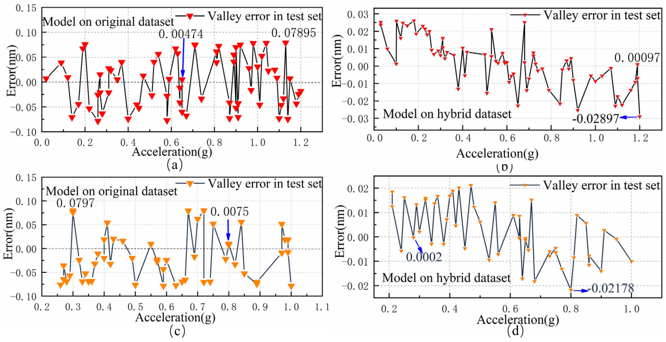

Fig. 19. Valley error comparison at 20 and 40 Hz for original versus hybrid datasets. Error distributions for (a) original dataset (4–78 pm) and (b) hybrid dataset (1–26 pm). Error distributions for (c) original dataset (7–80 pm) and (d) hybrid dataset (0.2–21 pm).

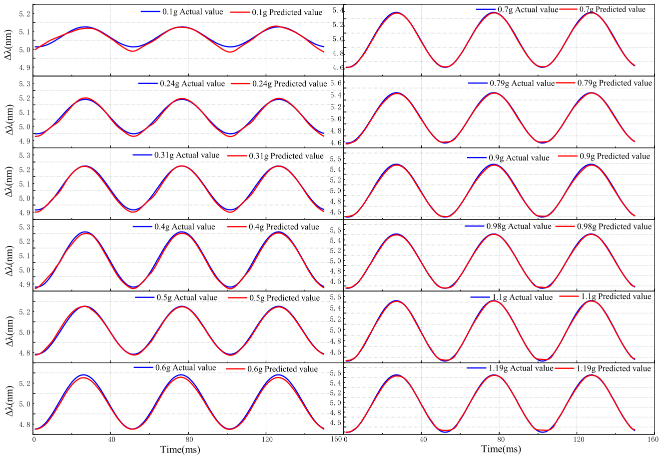

Fig. 20. CNN–BiLSTM–Attention prediction results for 20-Hz vibrations in a mixed testing set.

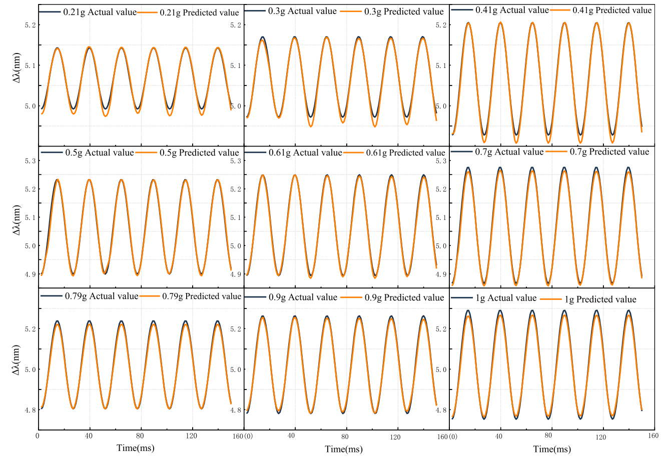

Fig. 21. CNN–BiLSTM–Attention prediction results for 40-Hz vibrations in a mixed testing set.

To evaluate the performance of the CNN–BiLSTM–Attention model in dynamic spectral prediction, we employed four metrics—mean absolute percentage error (MAPE), coefficient of determination (R^2), mse, and MAE. These metrics are defined as follows [42]:

$$
\begin{aligned}
\text{mse} &= \frac{1}{m}\sum_{i=1}^{m}(y_i - \hat{y}_i)^2 \\
\text{MAE} &= \frac{\sum_{i=1}^{m}\left|y_i - \hat{y}_i\right|}{m} \\
R^2 &= 1 - \frac{\sum_i (y_i - \hat{y}_i)^2}{\sum_i (\bar{y}_i - y_i)^2} \\
\text{MAPE} &= \frac{1}{m}\sum_{i=1}^{m}\left|\frac{\hat{y}_i - y_i}{y_i}\right|
\end{aligned}
\tag{14}
$$

where y_i denotes the actual wavelength difference, $\hat{y}_i$ denotes the predicted wavelength difference, $\bar{y}_i$ denotes the mean of the actual wavelength difference, and m denotes the total number of test samples. As shown in Table II, PR–NLR, which does not use DL, performs substantially worse than the DL approaches, underscoring the strong capability of DL-based models to extract and fit complex spectral features. For a fair comparison, the proposed CNN–BiLSTM–Attention model was evaluated alongside LSTM, CNN–LSTM, and CNN–BiLSTM, all trained on the same dataset and subjected to identical preprocessing, random partitioning, and data augmentation procedures. A detailed analysis reveals that each architectural enhancement in the DL models contributed progressively to performance gains. Replacing LSTM with CNN-LSTM reduced mse by 70% (from 29.69×10^{-4} to 8.87×10^{-4}) by leveraging spatial feature extraction, while bidirectional LSTM (BiLSTM) further lowered mse by 60% (from 8.87×10^{-4} to 3.58×10^{-4}) through improved temporal modeling. This indicates the progressively enhanced ability of convolutional layers and bidirectional LSTM units to capture the temporal features of spectral data.

Building upon CNN–BiLSTM, the integration of an attention mechanism provided further improvements: the mse dropped by 25% (from 3.58×10^{-4} to 2.67×10^{-4}), MAE by 26% (from 1.135×10^{-2} to 0.844×10^{-2}), and MAPE by 42% (from 3.992×10^{-2} to 2.296×10^{-2}), while R^2 rose to 0.98933. Hierarchically, attention refines feature extraction at

TABLE II
PERFORMANCE METRICS STATISTICS FOR PR–NLR, LSTM, CNN–LSTM, CNN–BILSTM, CNN–BILSTM–ATTENTION

Model	MSE($\times10^{-4}$)	MAE($\times10^{-2}$)	MAPE($\times10^{-2}$)	R^2
PR-NLR	94.63	8.5	1.63	0.81
LSTM	29.68966	3.051	8.013	0.91034
CNN-LSTM	8.86509	2.095	5.685	0.96459
CNN-BiLSTM	3.5829	1.135	3.992	0.97314
CNN-BiLSTM-Attention	2.67019	0.844	2.296	0.98933

multiple levels by filtering noise at the CNN layer, prioritizing temporal dependencies in the BiLSTM layer, and emphasizing critical wavelength regions at the output layer. This multilevel attention strategy collectively enhances robustness against noise and provides a more accurate representation of critical features, thereby yielding significant gains in spectral prediction accuracy.

Overall, these results confirm that DL models significantly outperform non-DL methods in handling complex spectral data and those attention mechanisms—when applied at various levels—greatly enhance predictive accuracy and robustness. This is crucial for real-world applications where small inaccuracies in wavelength measurement can lead to large uncertainties in structural health monitoring or high-frequency vibration assessments.

V. CONCLUSION

This article proposed and validated two dynamic spectral reconstruction models based on AWGs for differential FBG accelerometers. First, an equal-strength triangular cantilever beam accelerometer was designed with two symmetrically fixed FBGs, enhancing acceleration sensitivity and eliminating temperature crosstalk through differential detection. An AWG-based PR–NLR model enabled dynamic wavelength demodulation under varying acceleration frequencies, achieving an error range of 4–82 pm—slightly lower in accuracy than HSD, but with notable advantages in integration, cost-effectiveness, and multichannel multiplexing.

Second, a CNN–BiLSTM–Attention model, combined with GAN-based data augmentation, reduced spectral prediction errors to 1–26 pm at 20 Hz and 0.2–21 pm at 40 Hz, demonstrating excellent generalization and precision in dynamic scenarios. The proposed DL framework reduces prediction errors by up to 89.93% compared with the PR–NLR method, with MAE decreasing from 3.99×10^{-2} to 0.91×10^{-2} nm at 20 Hz and from 3.25×10^{-2} to 0.81×10^{-2} nm at 40 Hz. These improvements highlight the critical role of DL in addressing noise susceptibility and temporal dependency challenges inherent in dynamic environments.

Regarding deployment, the DL model requires moderate computational resources (e.g., a GPU for real-time inference) and operates effectively at frequencies up to 40 Hz, with a sampling interval of 150 ms per prediction cycle. While the experiments were constrained by the vibration table's frequency limits, the architecture's bidirectional temporal modeling and attention mechanisms ensure scalability to higher frequencies with optimized hardware acceleration. The system's lower frequency threshold is determined by the sensor's natural frequency (28.44 Hz), below which mechanical damping reduces sensitivity. However, the DL framework remains adaptable to broader operational ranges by incorporating domain-specific data augmentation and transfer learning.

Although the AWG-based solution does not match HSD in absolute accuracy, it offers robust performance in resource-constrained scenarios, such as structural health monitoring, where cost and integration outweigh ultrahigh precision. Future work will focus on validating the framework at extended frequencies and integrating edge-computing platforms for real-time industrial deployment.

ACKNOWLEDGMENT

Qian Yang is with the College of Electronic Science and Technology, School of Information and Communication Engineering, Hainan University, Haikou 570228, China, and also with the School of Electrical Engineering, Henan Mechanical and Electrical Vocational College, Zhengzhou 451100, China (e-mail: iamyangqianw@126.com).

Lei Liu, Ning Niu, ChenYi Quan, SuFen Ren, YuMeng Yan, and LongTeng Xiang are with the College of Electronic Science and Technology, School of Information and Communication Engineering, Hainan University, Haikou 570228, China (e-mail: lei0824lei@163.com; niuning@hainanu.edu.cn; 1440529604@qq.com; rsf18854752905@163.com; yanyumeng0502@163.com; 19860951162@163.com).

ShengChao Chen is with the School of Computer Science, Faculty of Engineering and Information Technology, University of Technology Sydney, Sydney, NSW 2007, Australia (e-mail: pavelchen@ieee.org).

JiaLin Zhang and GuanJun Wang are with the College of Electronic Science and Technology, Hainan University, Haikou 570228, China (e-mail: jialinzhang@hainanu.edu.cn; wangguanjun@hainanu.edu.cn).

YiPing Wang, ChangRui Liao, and Jun He are with the School of Physics and Optoelectronic Engineering, Shenzhen University, Shenzhen 518060, China (e-mail: ypwang@szu.edu.cn; cliao@szu.edu.cn; hejun07@szu.edu.cn).

REFERENCES

[1] T. T.-V. Nguyen, H.-D. Le, H.-C. Hsu, C.-N. Nguyen, and C.-C. Chiang, "A medium-high frequency FBG accelerometer based on a V-shaped flexible Hinge," *Measurement*, vol. 224, Jan. 2024, Art. no. 113865.

[2] W. Udos, Y.-S. Lee, K.-S. Lim, Z.-C. Ong, M. K. A. Zaini, and H. Ahmad, "Signal enhancement of FBG-based cantilever accelerometer by resonance suppression using magnetic damper," *Sens. Actuators A, Phys.*, vol. 304, Apr. 2020, Art. no. 111895.

[3] S. M. Nizar and B. E. Caroline, "Comparison of fiber optic sensors based on FBG—A review," in *Proc. IEEE Int. Conf. Syst., Comput., Autom. Netw. (ICSCAN)*, Mar. 2019, pp. 1–6.

[4] Y. Guo, M. Chen, L. Xiong, X. Zhou, and C. Li, "Fiber Bragg grating based acceleration sensors: A review," *Sensor Rev.*, vol. 41, no. 1, pp. 101–122, Feb. 2021.

[5] T. Li, J. Guo, Y. Tan, and Z. Zhou, "Recent advances and tendency in fiber Bragg grating-based vibration sensor: A review," *IEEE Sensors J.*, vol. 20, no. 20, pp. 12074–12087, Oct. 2020.

[6] F. Chen, X. Li, R. Wang, and X. Qiao, "Sensitivity enhancement of fiber-optic accelerometers using thin-cladding fiber Bragg gratings," *J. Lightw. Technol.*, vol. 39, no. 18, pp. 5988–5994, Sep. 18, 2021.

[7] N. Basumallick, P. Biswas, K. Dasgupta, and S. Bandyopadhyay, "Design optimization of fiber Bragg grating accelerometer for maximum sensitivity," *Sens. Actuators A, Phys.*, vol. 194, pp. 31–39, May 2013.

[8] H.-D. Le, C.-C. Chiang, C.-N. Nguyen, and H.-C. Hsu, "A novel short fiber Bragg grating accelerometer based on a V-type dual mass block structure for low- and medium-frequency vibration measurements," *Opt. Laser Technol.*, vol. 161, Jun. 2023, Art. no. 109131.

[9] A. Dandridge and A. B. Tveten, "Phase compensation in interferometric fiber-optic sensors," *Opt. Lett.*, vol. 7, no. 6, p. 279, 1982.

[10] R. Wang, Y. Li, and X. Qiao, "Recent advances in multidimensional fiber Bragg grating accelerometers," *J. Lightw. Technol.*, vol. 41, no. 13, pp. 4238–4247, Jul. 1, 2023.

[11] R. Wang, T. Li, S. Gong, and X. Qiao, "Multicore fiber based phase-modulation interferometer for demodulation of a fiber Bragg grating accelerometer," *J. Lightw. Technol.*, vol. 42, no. 5, pp. 1765–1769, Mar. 1, 2024.

[12] L. Li et al., "The study of fiber Bragg grating demodulating technology based on unbalanced MZ interferometer," *Piezoelectr. Acoustoopt.*, vol. 30, no. 1, pp. 16–18, 2008.

[13] Y. E. Marin et al., "Integrated dynamic wavelength division multiplexed FBG sensor interrogator on a silicon photonic chip," *J. Lightw. Technol.*, vol. 37, no. 18, pp. 4770–4775, Sep. 15, 2019.

[14] T. Li, R. Wang, and X. Qiao, "Demodulation of fiber Bragg grating accelerometer using in-line Sagnac interferometers," *IEEE Sensors J.*, vol. 22, no. 5, pp. 4077–4082, Mar. 2022.

[15] T. Li, F. Chen, R. Wang, and X. Qiao, "Improved phase generated carrier demodulation for time-division multiplexed FBG accelerometers," *J. Lightw. Technol.*, vol. 43, no. 2, pp. 942–947, Jan. 15, 2025.

[16] G. Yao, B. Yan, B. Li, Y. Wu, Z. Zong, and Y. Li, "Highly precise FBG wavelength demodulation method with strong multiplexing ability and positioning function based on time-domain detection," *Opt. Exp.*, vol. 32, no. 7, pp. 12708–12723, 2024.

[17] J. Koch, M. Angelmahr, and W. Schade, "Arrayed waveguide grating interrogator for fiber Bragg grating sensors: Measurement and simulation," *Appl. Opt.*, vol. 51, no. 31, pp. 7718–7723, 2012.

[18] J. Alves, J. L. Santos, A. Carvalho, and A. Lage, "Fiber Bragg sensor interrogation system based on a CCD spectrometer," in *Proc. IEEE SENSORS*, Oct. 2003, pp. 909–913.

[19] T. H. T. Chan et al., "Vertical displacement measurements for bridges using optical fiber sensors and CCD cameras—A preliminary study," *Struct. Health Monit.*, vol. 8, no. 3, pp. 243–249, May 2009.

[20] A. D. Kersey, T. A. Berkoff, and W. W. Morey, "Multiplexed fiber Bragg grating strain-sensor system with a fiber Fabry–Pérot wavelength filter," *Opt. Lett.*, vol. 18, no. 16, pp. 1370–1372, Aug. 1993.

[21] Y. Xu, H. Qi, X. Zhao, C. Li, and K. Chen, "High-speed spectrum demodulation of fiber-optic Fabry–Pérot sensor based on scanning laser," *Opt. Lasers Eng.*, vol. 178, Mar. 2024, Art. no. 108192.

[22] W. Yuan et al., "A high-speed scanning module based on a DBR tunable laser for FBG sensor systems," in *Proc. 24th Int. Conf. Transparent Opt. Netw. (ICTON)*, Jul. 2024, pp. 1–4.

[23] M. Dastmalchi, S. Doucet, L. A. Rusch, and S. LaRochelle, "FBG-based matched filters for optical processing of RF signals," *IEEE Photon. J.*, vol. 4, no. 3, pp. 832–843, Jun. 2012.

[24] R. Soman, F. O. Moaf, P. Fiborek, P. Kudela, and M. Kurpińska, "Investigating the suitability of the matched fiber Bragg grating approach for guided wave based structural health monitoring," *Measurement*, vol. 242, Jan. 2025, Art. no. 115935.

[25] M. A. Davis and A. D. Kersey, "Matched-filter interrogation technique for fibre Bragg grating arrays," *Electron. Lett.*, vol. 31, no. 10, pp. 822–823, May 1995.

[26] L. Lei, Z. Yuning, D. Shangming, and T. Xiaoling, "High speed demodulation of FBG based on variable step scanning strategy," *Infr. Laser Eng.*, vol. 53, no. 4, 2024, Art. no. 20230671.

[27] M. Li, Y. Huang, R. Wang, and X. Qiao, "On-chip cascaded micro-ring filters for demodulation of multiplexed FBG accelerometers," *Opt. Lett.*, vol. 50, no. 2, pp. 337–340, 2025.

[28] D. Robertson, P. Niewczas, and J. R. McDonald, "Interrogation of a dual-fiber-Bragg-grating sensor using an arrayed waveguide grating," *IEEE Trans. Instrum. Meas.*, vol. 56, no. 6, pp. 2641–2645, Dec. 2007.

[29] P. Yuan, S. Weng, S. Ji, D. Zhang, and L. Zhu, "Performance analysis of fiber Bragg grating sensor interrogators based on arrayed waveguide gratings," *Opt. Eng.*, vol. 60, no. 6, Jun. 2021, Art. no. 066101.

[30] J. Zhang et al., "Arrayed waveguide grating-based high-frequency ultrasonic sensors," *Proc. SPIE*, vol. 11191, pp. 65–71, Nov. 2019.

[31] L. Meng, H. Wang, Q. Xia, T. Yuan, X. Zhang, and L. Yuan, "In-fiber thermally diffused coupler and fiber Bragg grating inscribed in twin-core fiber for sensitivity-enhanced vector bending sensing," *Photon. Sensors*, vol. 13, no. 3, 2023, Art. no. 230310.

[32] J. Zhang, C. Tao, J. Xiao, Y. Zhao, and X. Jiang, "Dynamic strain sensing system using a SOA based fiber ring laser with fiber Bragg gratings and an AWG demodulator," *Proc. SPIE*, vol. 11593, pp. 48–53, Mar. 2021.

[33] A. Venketeswaran et al., "Recent advances in machine learning for fiber optic sensor applications," *Adv. Intell. Syst.*, vol. 4, no. 1, Jan. 2022, Art. no. 2100067.

[34] C. Wei, Q. Liu, Y. Wang, D. Zhu, J. Shi, and D. Lin, "Accurate strain sensing with fiber-optic Fabry–Pérot sensors based on CNN-LSTM model," *IEEE Sensors J.*, vol. 24, no. 11, pp. 17725–17732, Jun. 2024.

[35] Z. Yue, W. Li, D. Zheng, C. Xie, W. Pan, and X. Zou, "Performance enhancement of arrayed waveguide grating-based fibre Bragg grating interrogation assisted by random forest," *Electron. Lett.*, vol. 59, no. 1, Jan. 2023, Art. no. e12682.

[36] B. Li et al., "High performance AWG-based FBG interrogator using cascaded neural network," *J. Lightw. Technol.*, vol. 42, no. 24, pp. 8802–8810, Dec. 15, 2024.

[37] M. A. Jucá and A. B. D. Santos, "Fiber Bragg grating interrogation using FBG filters and artificial neural network," in *IEEE MTT-S Int. Microw. Symp. Dig.*, Aug. 2017, pp. 1–4.

[38] M. Méndez, M. G. Merayo, and M. Núñez, "Long-term traffic flow forecasting using a hybrid CNN-BiLSTM model," *Eng. Appl. Artif. Intell.*, vol. 121, May 2023, Art. no. 106041.

[39] P. K. Shrivastava, M. Sharma, P. Sharma, and A. Kumar, "HCBiLSTM: A hybrid model for predicting heart disease using CNN and BiLSTM algorithms," *Meas., Sensors*, vol. 25, Feb. 2023, Art. no. 100657.

[40] Z. Ma, Y. Sun, H. Ji, S. Li, S. Nie, and F. Yin, "A CNN-BiLSTM-attention approach for EHA degradation prediction based on time-series generative adversarial network," *Mech. Syst. Signal Process.*, vol. 215, Jun. 2024, Art. no. 111443.

[41] B. Hou et al., "Differential fiber grating vector flow velocity sensor based on strain amplifying cantilever beam structure," *IEEE Sensors J.*, vol. 22, no. 23, pp. 22678–22690, Dec. 2022.

[42] H. Xu, S. Chen, S. Ren, X. Hou, G. Wang, and C. Shen, "Dual-parameter demodulation of FBG-FPI cascade sensors via sparse samples: A deep learning-based perspective," *IEEE Sensors J.*, vol. 23, no. 19, pp. 23903–23915, Oct. 2023.